Sustainable Energy & Fuels

Steam Reforming of Methane by Titanium oxide Photocatalysts with Hollow Spheres

Journal:	*Sustainable Energy & Fuels*
Manuscript ID	SE-ART-10-2023-001346.R1
Article Type:	Paper
Date Submitted by the Author:	18-Dec-2023
Complete List of Authors:	Yamaguchi, Akira; Tokyo Kogyo Daigaku, Kujirai, Tomoki; Tokyo Kogyo Daigaku, Fujita, Takeshi; KUT, School of Engineering Science Abe, Hideki; National Institute for Materials Science, Hydrogen Production Miyauchi, Masahiro; Tokyo Institute of Technology, Graduate School of Science and Engineering

ARTICLE

Steam Reforming of Methane by Titanium oxide Photocatalysts with Hollow Spheres

Received 00th January 20xx,
Accepted 00th January 20xx

DOI: 10.1039/x0xx00000x

Akira Yamaguchi,[*a] Tomoki Kujirai,[a] Takeshi Fujita,[b] Hideki Abe[c] and Masahiro Miyauchi[*a]

Steam reforming of methane (SRM) is one of the most useful techniques for methane (CH_4) conversion because of the large hydrogen yield per CH_4 molecule. However, this process is not commercially viable due to the high reaction temperature and associated energy costs. To decrease the SRM reaction temperature, the introduction of photochemical energy has been proposed; however, the charge recombination of photo-generated carriers must be suppressed to achieve higher activity. Here, TiO_2 photocatalysts with a hollow sphere structure are synthesized and loaded with spatially separated co-catalysts to achieve high charge separation in an attempt to improve SRM efficiency. The highest SRM activity is observed for hollow-sphere structured TiO_2 with Pt and Rh_2O_3 co-catalysts selectively deposited on the inner and outer TiO_2 surfaces, respectively. In-situ electron spin resonance and photo-luminescence measurements clearly demonstrate that photo-excited electrons and holes are trapped at Pt and Rh_2O_3 sites, respectively, of Rh/hollow TiO_2/Pt, resulting in efficient charge separation and increased SRM activity. Taken together, these findings support our hypothesis that the spatial separation and heterogeneous loading of co-catalysts is a promising design strategy for photocatalytic methane conversion reactions.

Introduction

Methane (CH_4) is an earth-abundant natural resource found in natural and shale gases and in the form of methane hydrate; however, CH_4 is recognized as a major greenhouse gas with the second largest contribution to emissions behind carbon dioxide (CO_2)[1]. According to the U. S. Energy Information Administration, the production of dry natural gas is increasing annually with the aid of recent advances in mining technology and predicted to exceed 35 tcf by 2025[2]. To utilize CH_4 as an energy resource, several CH_4 conversion techniques, such as dry reforming of methane (DRM: $CH_4 + CO_2 \rightarrow 2CO + 2H_2$, ΔH_{298K} = +247 kJ/mol), steam reforming of methane (SRM: $CH_4 + H_2O \rightarrow CO + 3H_2$, ΔH_{298K} = +205 kJ/mol) and partial oxidation of methane (POM: $CH_4 + 1/2O_2 \rightarrow CO + 2H_2$, ΔH_{298K} = −38 kJ/mol) have been developed[3,4 5]. Among these techniques, SRM generates the highest amount of hydrogen (H_2), which is widely used as a fuel and feedstock for methanol and ammonia production, from one CH_4 molecule. The SRM process has been industrialized to produce H_2[6,7] and generates approximately half of the H_2 used worldwide is[8]. However, because SRM is a highly endothermic reaction and requires a high reaction temperature (>800 ℃), nickel (Ni) and ruthenium (Ru)-based catalysts have been adopted to facilitate industrial SRM reactions [9–11], while CH_4 can be reformed at the temperature range of 350 - 450 K by lowering the pressure to 10^{-5} Pa [12].

One strategy to promote SRM at lower temperatures is the utilization of photocatalysts to harness solar energy [13]. The current challenge and future prospects of photocatalysis systems are summarized in recent review articles[14,15]. Our group has explored photocatalytic DRM using various kinds of photocatalysts[16–22]. For example, Shoji et al.[18] demonstrated that Rh/$SrTiO_3$ catalyzes DRM under ultraviolet (UV) irradiation with a conversion efficiency that cannot be achieved by thermal reaction[18]. Additionally, isotope experiments showed that the O^{2-} ion in $SrTiO_3$ functions as a reaction mediator between the oxidation ($CH_4 + O^{2-} \rightarrow CO + 2H_2 + 2e^-$) and reduction ($CO_2 + 2e^- \rightarrow CO + O^{2-}$) reactions during the DRM process. In addition, Cho et al. demonstrated photocatalytic DRM under visible-light irradiation using Rh/TaON as a photocatalyst[19]. Photo-promoted SRM has been also examined by other research groups,[23–35] including Yoshida et al., who first reported photocatalytic SRM using Pt/TiO_2[24]. Although photocatalytic DRM and SRM is thought to proceed via bandgap excitation, the photo-assistance of a photo-excited hot carrier in the metal nanoparticles of the catalysts is also proposed to promote photocatalytic SRM[36]. Although these reports have shown that photo-promoted SRM is a useful strategy to promote CH_4 conversion under ambient temperature and pressure, the use of particle-type catalysts is an obstacle for clarifying the SRM reaction mechanism due to the existence of oxidation and reduction sites on the same particle.

To study photocatalytic DRM, our group recently constructed a gas-phase photoelectrochemical (GPEC) system to separate the CH_4 oxidation and CO_2 reduction sites using an oxygen ion-conductive solid electrolyte [20]. The separation of catalytic active sites in the GPEC

[a] School of Materials and Chemical Technology, Tokyo Institute of Technology, 2-12-1 Ookayama, Meguro-ku, Tokyo 152-8552, Japan.
[b] School of Engineering Science, Kochi University of Technology, 185 Miyanokuchi, Tosayamada, Kami, Kochi 782-8502, Japan.
[c] National Institute for Materials Science, 1-1 Namiki, Tsukuba, Ibaraki 305-0044, Japan.

Electronic Supplementary Information (ESI) available: FE-TEM image, N_2 adsorption-desorption isotherm, XPS spectra, and optical properties of samples, SRM activity dependence on co-catalyst loading amount and temperature, spectrum of light for SRM test, and schematic image of reactor. See DOI: 10.1039/x0xx00000x

system allowed for the design of DRM photocatalysts with improved activity and also suppression of unwanted SRM side reactions, such as CO_2 generation. Using a GPEC system with an Pt catalyst, we demonstrated that CO and H_2 were produced stoichiometrically, indicating that side-reactions were effectively suppressed[37]. The application of GPEC systems revealed that efficient SRM requires suppression of the recombination of photo-excited holes and electrons, site separation for oxidation/reduction reactions, and modification with appropriate co-catalysts for H_2O reduction and CH_4 oxidation reactions.

In the present work, a photocatalyst with a hollow sphere structure to allow for reaction site separation was applied for SRM. The hollow sphere-structure permits loading different co-catalysts on the inner and outer surfaces of the photocatalyst, thereby achieving active site separation and suppression of charge recombination[38, 39]. The thin wall of shell structure also contributes to charge separation. Although photocatalysts with a hollow sphere structure efficiently promote water splitting reactions[4,40–45] and CO_2 reduction[46], the applicability of such catalysts towards photocatalytic SRM remains unclear. Here, hollow sphere-structured TiO_2 was selected as a representative photocatalyst and was loaded with Pt and Rh_2O_3 as co-catalysts to promote H_2O reduction and CH_4 oxidation reactions, respectively, because Pt particles in contact with an oxide like CeO_2 have special electronic and chemical properties[47, 48], enabling activation of CH_4 at temperatures below 500 K[49]. To elucidate the photocatalytic SRM reaction mechanism on hollow-structured TiO_2, the wavelength and temperature dependence of the SRM activity was examined in combination with spectroscopic techniques, including electron-spin resonance (ESR) and photo-luminescence (PL) spectroscopy.

Results and Discussion

Material Synthesis

Preparation of TiO_2 with a hollow sphere structure and loaded with a co-catalyst was performed using the template method reported by Ao et al.[50] (**Scheme 1**). First, a carbon sphere that served as a hollow template was synthesized using a hydrothermal method. Briefly, 6.0 g glucose (Kanto Chemical Co., Inc.) was dissolved into 60 mL distilled water and was then subjected to hydrothermal treatment at 180 °C for 12 h. The resulting product was collected by centrifugation and washed thoroughly with distilled water and ethanol. After drying the sample at 70 °C, the target carbon spheres were obtained and stored at room temperature until needed.

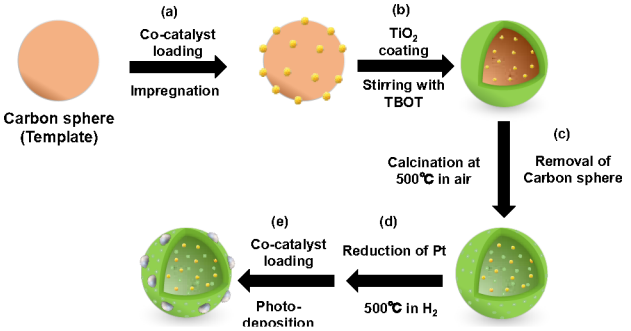

Scheme 1. Preparation of hollow sphere-structured TiO_2 loaded with Pt and Rh co-catalysts by impregnation and photodeposition methods, respectively.

To load Pt co-catalysts on the inner surfaces of the synthesized hollow sphere-structured TiO_2, Pt was deposited on the surface of the carbon spheres by an impregnation method (Scheme 1, step a). Hexachroloplatinum(IV) acid (H_2PtCl_6•$6H_2O$, Kanto Chemical Co., Inc.) with the desired target weight ratio to TiO_2 was mixed with carbon spheres in distilled water, and the mixture was then heated to 90 °C under stirring until the solvent was completely evaporated. The obtained material was ground into fine powder with an agate mortar and pestle and 0.1 g powder was then suspended into 20 mL ethanol into which 1 mL titanium (IV) tetrabutoxide ($Ti[O(CH_2)_3CH_3]_4$, TBOT, Wako Pure Chemical Industries, Ltd.) was added dropwise under stirring. The vessel was sealed with Parafilm and the suspension was stirred vigorously for 1 h. The product was collected with centrifugation, washed with ethanol, and dried at room temperature overnight. Further drying at 70 °C for 2 h resulted in the formation of TiO_2-coated carbon spheres (Scheme 1, step b). The template carbon spheres were removed by calcination at 500 °C in air for 3 h to obtain hollow sphere-structured TiO_2 (Scheme 1, step c). To reduce the Pt co-catalyst to the metallic phase, the sample was treated with H_2 (flow rate of 60 mL/min) in a tube furnace at 500 °C for 2 h (Scheme 1, step d). The loading of co-catalyst on the outer surfaces of the hollow sphere-structured TiO_2 was conducted using a photo-deposition method (Scheme 1, step e). Briefly, Pt-loaded hollow sphere-structured TiO_2 was suspended in rhodium chloride (III) ($RhCl_3$•$3H_2O$, Kanto Chemical Co., Inc.) aq. with the desired ratio of Rh and Ti, and the suspension was then irradiated with UV light for 5 min using an Hg-Xe lamp (A-410UV-5, Hayashi-Repic Co., Ltd.). Rh deposition on the outer surfaces of hollow sphere-structured TiO_2 was completed by an additional 15 min of UV irradiation in the presence of ethanol as a sacrificial reagent. The sample was then collected by centrifugation and dried at 70 °C in air.

As a control sample, hollow sphere-structured TiO_2 loaded with Rh and Pt co-catalysts on the inner and outer surfaces of spheres, respectively, was also prepared. Samples loaded with co-catalysts on the outer surfaces by the impregnation method were treated with H_2 at a flow rate of 60 ml/min at 500 °C for 2 h to reduce the co-catalyst. TiO_2 without a hollow sphere structure was also synthesized with the identical procedure except for the absence of the carbon sphere template. The loading amount of co-catalyst was 1 wt% unless otherwise noted. Hereafter, the samples are referred to as (outer surface co-catalyst)/hollow TiO_2/(inner surface co-catalyst). For example, the hollow sphere-structured TiO_2 sample loaded with Rh and Pt on the outer and inner surfaces, respectively, is referred to as Rh/hollow TiO_2/Pt.

Characterization of the hollow sphere-structured TiO_2 samples

The crystal structures of the hollow sphere-structured TiO_2 samples were examined by XRD and all observed peaks were assignable to anatase TiO_2 (ICDD No. 00-021-1271; **Figure 1a**). Even after the loading of co-catalysts onto TiO_2, the anatase structure was retained and no peaks assignable to the co-catalysts were observed, likely due

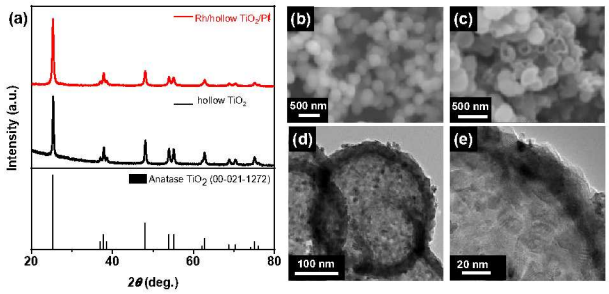

Figure 1. Characterization of the hollow sphere-structured TiO_2 samples. (a) XRD patterns and SEM images of the (b) carbon sphere template and (c) hollow sphere-structured TiO_2. Panels (d) and (e) are FE-TEM images of Rh/hollow TiO_2/Pt with different magnification.

to the high dispersion and/or low loading amount of the Rh/Pt nanoparticles. The diameters of the template carbon spheres and hollow sphere-structured TiO_2 were determined by SEM to range from 250~300 nm (Figure 1b and 1c). The hollow sphere structure was confirmed by FE-TEM observation (Figure 1d and e). The thickness of the shell of Rh/hollow TiO_2/Pt was determined to be 20~25 nm based on the sharp contrast between the hollow center and shell of the TiO_2 spheres.

The presence of the co-catalysts in the hollow sphere-structured TiO_2 was confirmed by elemental mapping and FE-TEM (**Figure S1**). The FT-TEM imaging revealed that both the Rh and Pt co-catalysts were highly distributed on the hollow sphere-structured TiO_2. The elemental mapping of Ti in the Rh/hollow TiO_2/Pt sample also supports the photocatalyst contained a hollow sphere structure. The separation of the Rh and Pt co-catalysts onto the outer and inner surfaces, respectively, of hollow sphere-structured TiO_2 was confirmed by STEM observation, elemental mapping, and AES (**Figure 2**). Elemental mapping in the STEM image showed that Pt was homogeneously distributed on the inner surface of the shell in the form of nanoparticles with diameters of 1-2 nm, whereas Rh nanoparticles with diameters of 10-15 nm were deposited on the outer surface of TiO_2 (Figure 2a). In the AES measurements, Rh and Ti signals were observed, but Pt was not detected (Figure 2b). As the AES measurement has high sensitivity for surfaces (2 nm in depth from the surface), these results clearly indicate that Pt was deposited on the inner surface of the hollow sphere structure of TiO_2, whereas Rh was deposited on the outer surface.

N_2 adsorption-desorption isotherms were measured for the hollow TiO_2 and Rh/hollow TiO_2/Pt samples to gain insight into the mesoporous structure of hollow TiO_2 (**Figure S2**). In the N_2 adsorption-desorption isotherm of hollow TiO_2, a type-IV isotherm with a H3-type hysteresis loop[51] was observed (Figure S2a), indicating the presence of meso pores with diameters ranging from 2 to 50 nm and a peak maximum of 3.3 nm for the pore size distribution (Figure S2a, inset). The same feature was observed for Rh/Hollow TiO_2/Pt with only slight differences in the peak maximum (3.5 nm) of the pore size distribution (Figure S2b). The presence of meso pores would support diffusion of the gas substrate from outside of the hollow sphere TiO_2 structure to the inner active site, thereby increasing photocatalytic activity. The BET surface areas of

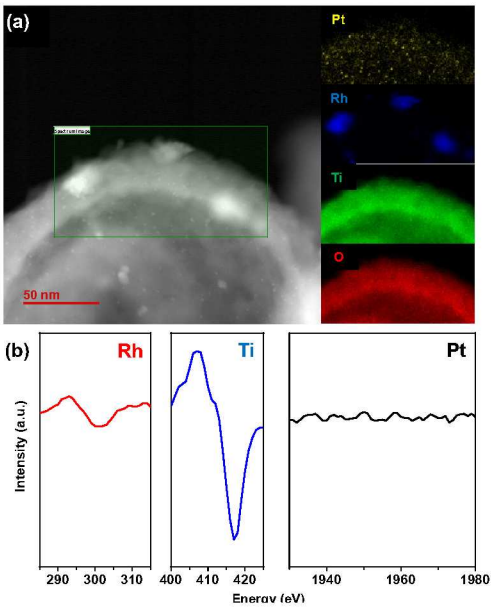

Figure 2. Surface analysis of the Rh/hollow TiO_2/Pt sample. (a) STEM image with elemental mapping and (b) Auger electron spectra. The inset in (a) represents the elemental mapping for Pt, Rh, Ti and O within the green box in the SEM image.

the hollow TiO_2 and Rh/hollow TiO_2/Pt samples were determined to be 1.94 and 2.07 m^2/g, respectively.

The valence states of the loaded co-catalysts were analyzed by XPS (**Figure S3**). The XPS spectrum of Rh/hollow TiO_2/Pt in the Rh 3d region (Figure S3a) contains Rh $3d_{5/2}$ peaks at 307.0 and 309.0 eV, and Rh $3d_{3/2}$ peaks were observed at 311.7 and 313.7 eV. The peaks at 307.0 eV and 309.0 eV are assignable to Rh^0 and Rh^{3+}, respectively[52–54], indicating that metallic Rh and Rh_2O_3 were deposited on Rh/hollow TiO_2/Pt. A key process for Rh_2O_3 formation is the photodeposition of Rh in the presence of dissolved O_2. This process triggers not only the photoreduction of Rh ions, but also activation of O_2, which then reacts with Rh ions to form Rh_2O_3[55] . In contrast to Rh, the presence of dissolved O_2 did not affect the valence state of photodeposited Pt, because Pt is not easily reduced or oxidized[55]. The absence of oxidized Pt on Rh/hollow TiO_2/Pt was confirmed by the XPS spectrum in the Pt 4f region (Figure S3b), as only peaks for metallic Pt were observed (Pt $4f_{7/2}$: 71.2 eV, Pt $4f_{5/2}$: 74.5 eV)[56, 57]. Thus, all of the Pt deposited using an impregnation method was reduced to the metallic state by H_2 treatment. The valence state of Ti in Rh/hollow TiO_2/Pt was confirmed to be Ti^{4+} as two peaks corresponding to TI^{4+} (Ti $2p_{3/2}$: 458.7 eV, Ti $2p_{1/2}$: 464.5 eV) were observed in the XPS spectra in the Ti 2p region[58].

The optical properties of the hollow TiO_2 and Rh/hollow TiO_2/Pt photocatalysts was examined with UV-Vis absorption spectroscopy (**Figure S4**). In the obtained UV-Vis spectra of hollow TiO_2 and Rh/hollow TiO_2/Pt, similar absorption edges originating from bandgap excitation of TiO_2 were observed (Figure S4a). In addition to bandgap excitation absorption, Rh/hollow TiO_2/Pt exhibited strong absorption in the visible light region that corresponded to the plasmonic absorption of Rh/Pt. The bandgap value of hollow TiO_2 was estimated from the Tauc-plot to be 3.16 eV (Figure S4b), which is consistent with the reported bandgap value for anatase TiO_2 of 3.2 eV[59,60,61].

SRM activity test

The SRM test was next conducted with hollow TiO_2-based samples to demonstrate the active site separation was promising strategy for SRM activity enhancement (**Figure 3**). First, the SRM activity among samples with different co-catalyst loading methods was first compared. To evaluate the effect of the loading method, only Rh was used as a co-catalyst in this experiment. Here, a sample designation of "i" indicates that an impregnation method was applied to co-catalyst loading, whereas "pd" indicates that the co-catalyst was photodeposited. For example, Rh_pd/hollow TiO_2/Rh_i indicates Rh was loaded on the outer surface of hollow TiO_2 by photodeposition and an impregnation method was used to deposit Rh on the inner surface. The H_2 production rate for SRM using the various co-catalyst-loaded hollow TiO_2 photocatalysts was measured (Figure 3a). As the H_2 production activity of Rh_i/hollow TiO_2 was less than Rh_pd/hollow TiO_2, and Rh_i/hollow TiO_2/Rh_i was less than Rh_pd/hollow TiO_2/Rh_i, photodeposition appears to be the more suitable deposition method to achieve high SRM activity. The same tendency was observed for non-hollow TiO_2, as samples with photodeposited Rh had higher SRM activity than impregnated Rh co-catalyst samples (**Figure S5**). Further, the highest activity was observed for Rh_pd/hollow TiO_2/Rh_i, indicating that the hollow sphere structure contributed to the higher photocatalytic activity. The higher activity of the hollow sphere structure is likely attributable to the increased number of reaction sites resulting from deposition of co-catalysts on both of outer and inner surfaces of hollow TiO_2. Furthermore, because Rh_2O_3 was formed on the outer surface of hollow TiO_2, as revealed by the XPS analysis, and only metallic Rh was present on the inner surface by H_2 reduction, it was anticipated that charge recombination would be suppressed. Specifically, photogenerated electrons would tend to move to metallic sites on the inner surface and holes would relocate to Rh_2O_3 sites on the outer surface[55], thereby enhancing charge separation.

The effect of heterogeneous co-catalyst loading on SRM activity was examined by comparing the photocatalytic activity of hollow TiO_2 loaded with Rh and Pt as co-catalysts on the outer surface using photodeposition (Figure 3b). The SRM activities of Pt/hollow TiO_2/Rh and Pt/hollow TiO_2/Pt were lower than those of Rh/hollow TiO_2/Pt and Rh/hollow TiO_2/Rh, indicating the photodeposited Pt is not an efficient co-catalyst for SRM. In contrast, the highest SRM activity of 4.95 μmol/min was achieved with Rh/hollow TiO_2/Pt and was two times higher than that of Rh/hollow TiO_2/Rh (2.02 μmol/min). The outer quantum efficiency was calculated to be 3.51 % for H_2 production on Rh/hollow TiO_2/Pt. The detailed calculation procedure is described in Supporting Information. The apparent color of the samples didn't change after 3 hours of SRM test, indicating samples were free from deactivation by coking. As discussed above, the presence of a metallic co-catalyst on the inner TiO_2 surface and an oxidized co-catalyst on the outer surface enhanced charge separation. Because Pt has highest work function among noble metals, it is a suitable co-catalyst for capturing photogenerated electrons[62,63], resulting in more efficient charge separation and higher SRM activity than photocatalysts modified with only Rh-based co-catalysts. To further evaluate the stoichiometry of the reaction, the product distribution generated by Pt and Rh-loaded hollow TiO_2 photocatalysts during SRM was evaluated (**Figure S6**). The total amount of H_2 produced by both Rh/hollow TiO_2/Pt and Rh/hollow TiO_2/Rh was calculated based on the amounts of CO and CO_2 generated and equaled the expected sum from SRM ($CH_4 + H_2O \rightarrow CO + 3H_2$) and water gas shift ($CH_4 + 2H_2O \rightarrow CO_2 + 4H_2$) reactions, indicating that both reactions proceeded on these photocatalysts. Comparison of the production ratios of CO_2/H_2 and CO/H_2 by Rh/hollow TiO_2/Pt (0.090 and 0.22, respectively) and Rh/hollow TiO_2/Rh (0.11 and 0.20, respectively) suggests that the water gas shift reaction was suppressed on Rh/hollow TiO_2/Pt.

The dependence of the SRM activity on the co-catalyst loading amount was investigated for the Rh/hollow TiO_2/Pt sample (**Figure S7**). The influence of the Pt loading amount on photocatalytic SRM activity was examined by varying the amount of Pt loaded onto Rh/hollow TiO_2/Pt from 0.1 to 2.5 wt% and using 1.0 wt% Rh for all samples (Figure S7a). Notably, the 1.0 wt% Pt-loaded sample exhibited the highest SRM activity, whereas the other samples exhibited similar activities. Based on this result, the Rh loading amount was optimized for the 1.0 wt% Pt loaded sample (Figure S7b). The SRM activity increased as the Rh loading amount was increased from 0.1 to 1.0 wt%, but a slight decrease in activity was observed for the sample loaded with 2.5 wt% Rh. This tendency can be explained by the trade-off between an increase in active sites and the enhancement of photo-excited charge recombination. Overall, it was determined that the optimized loading amount for both Rh and Pt was of 1.0 wt%.

The temperature dependence of photocatalytic SRM activity on Rh/hollow TiO_2/Pt was next investigated. Under dark conditions (**Figure S8**, blue line), H_2 was not detected in the temperature range from 100 to 250 ℃, but H_2 was generated from 300 ℃. In contrast, under UV irradiation (Figure S8, red line), H_2 generation was detected at 100 ℃. Furthermore, the H_2 generation rate was higher under UV irradiation conditions in all temperature regions compared to dark conditions, indicating that a lower reaction temperature was permissible for uphill SRM under UV irradiation with the Rh/hollow TiO_2/Pt photocatalyst.

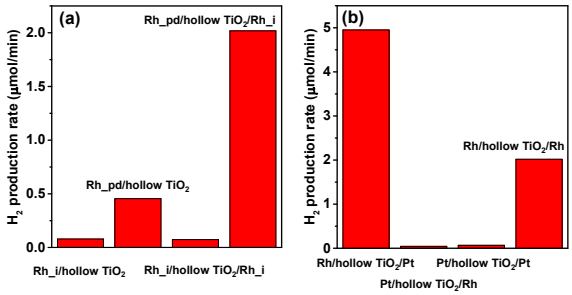

Figure 3. Photocatalytic SRM activity of hollow sphere-structured TiO_2 loaded with co-catalysts. (a) Comparison of the H_2 production rate by various Rh co-catalyst loading conditions and (b) between Rh and Pt as co-catalysts. The operation temperature was 300 ℃.

Examination of reaction mechanism

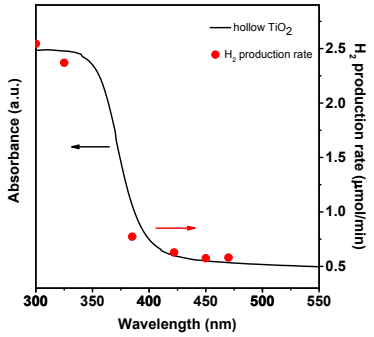

Figure 4. Wavelength dependence (action spectra) of photocatalytic SRM activity on Rh/hollow TiO_2/Pt, as measured by the H_2 production rate (red circles), plotted on the UV-Vis absorption spectrum of hollow TiO_2 (black line).

Before discussing the potential reaction mechanism of photocatalytic SRM on hollow TiO_2 system, the effect of photo-irradiation on surface temperature was evaluated (Figure S8). When Rh/hollow TiO_2/Pt was irradiated with UV light at an operation temperature of 300 ℃, the surface temperature increased to 396 ℃. Thus, the SRM activity at an operation temperature of 300 ℃ under UV irradiation (Figure S8, red line) was re-plotted against SRM activity at 396 ℃ (Figure S8, black line) and revealed that the H_2 production rate under UV irradiation was larger than that under dark conditions, even at the same surface temperature, over the entire temperature range examined. This result indicates that the enhancement of SRM activity by photo-irradiation of Rh/hollow TiO_2/Pt originated from not only a photothermal effect, but also due to a photocatalytic mechanism triggered by bandgap excitation of TiO_2.

To validate the possibility that a photochemical process contributed to the enhancement of SRM activity, the action spectrum of Rh/hollow TiO_2/Pt was examined. The wavelength dependence of photocatalytic SRM activity by Rh/hollow TiO_2/Pt was plotted on the UV-Vis absorption spectrum of hollow TiO_2 (**Figure 4**), showing that the action spectra was consistent with the absorption spectrum of hollow TiO_2. This finding indicates that the photo-generated electron-hole pairs resulting from bandgap excitation with UV irradiation are involved in the SRM on Rh/hollow TiO_2/Pt.

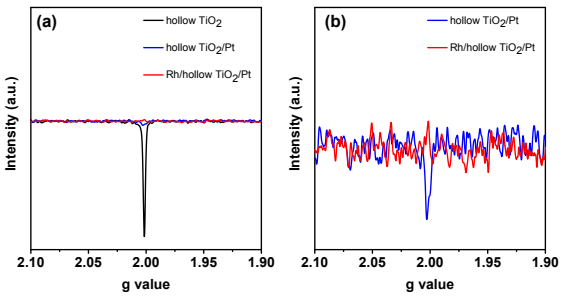

Figure 5. ESR spectra of hollow TiO_2 (black line), hollow TiO_2/Pt (blue line), and Rh/hollow TiO_2/Pt (red line) under N_2 and UV light irradiation. Panel (b) is an expanded image of panel (a).

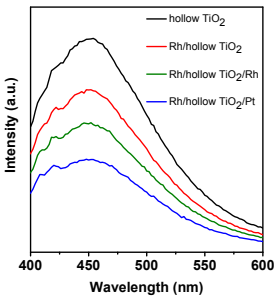

Figure 6. PL spectra for hollow TiO_2 photocatalysts loaded with Pt and Rh co-catalysts. Excitation wavelength = 380 nm.

To prove our hypothesis that the charge separation of photo-excited electron-hole pairs was promoted by the selective deposition of Pt and Rh_2O_3 co-catalysts on the inner and outer surfaces, respectively, of Rh/hollow TiO_2/Pt, in-situ ESR and PL measurements were conducted. The ESR spectra of hollow TiO_2, hollow TiO_2/Pt, and Rh/hollow TiO_2/Pt were measured under N_2 and UV light irradiation conditions (**Figure 5**). Under UV irradiation, hollow TiO_2 (Figure 5, black line) exhibited a large signal at g = 2.00, with the signal intensity being drastically decreased in this region for hollow TiO_2/Pt (Figure 5, blue line) and no signal was observed for Rh/hollow TiO_2/Pt (Figure 5, red line). This signal at g = 2.00 is assignable to O^- species[64–66], which originate from the capture of photo-excited holes by lattice O^{2-} [65]. In our previous work on photocatalytic SRM using Pt/Yttria-stabilized zirconia powder, we demonstrated that photo-excited holes were consumed in the CH_4 oxidation reaction[37]. The absence of an O^- signal for Rh/hollow TiO_2/Pt indicates that photo-excited holes were captured by Rh_2O_3 on the outer surface of Rh/hollow TiO_2/Pt, thereby suppressing the generation of O^- species. This result demonstrates that the presence of Rh_2O_3 on the outer TiO_2 surface contributed to the enhancement of charge separation by capturing photo-excited holes, resulting in the increased SRM activity observed for Rh/hollow TiO_2/Pt. The PL spectra for hollow TiO_2 photocatalysts loaded with co-catalysts and excited at 380 nm exhibited a peak intensity order of hollow TiO_2 > Rh/hollow TiO_2 > Rh/hollow TiO_2/Rh > Rh/hollow TiO_2/Pt (**Figure 6**). The peak intensity decrease in the PL spectra indicates that charge recombination between photo-excited electrons and holes had decreased [4]. Compared with bare hollow TiO_2 (Figure 6, black line), hollow TiO_2 loaded with co-catalyst exhibited lower peak intensity, indicating that the co-catalysts played important roles in charge separation. In the case of Rh/hollow TiO_2 (Figure 6, red line), both metallic Rh and Rh_2O_3 were present on the outer surface and served as electron- and hole-capturing sites, respectively. Although Rh sites would promote charge separation, adjacent sites between metallic Rh and Rh_2O_3 can serve as recombination sites, resulting in the larger PL peak intensity that was observed for Rh/hollow TiO_2 compared to that of Rh/hollow TiO_2/Rh (Figure 6, green line). In Rh/hollow TiO_2/Rh, Rh particles were deposited on both the inner and outer surfaces, and the inner Rh particles were reduced to the metallic state by H_2 treatment. As discussed previously, because Pt is more suitable as an electron-capturing site than Rh, Rh/hollow TiO_2/Pt exhibited the lowest PL

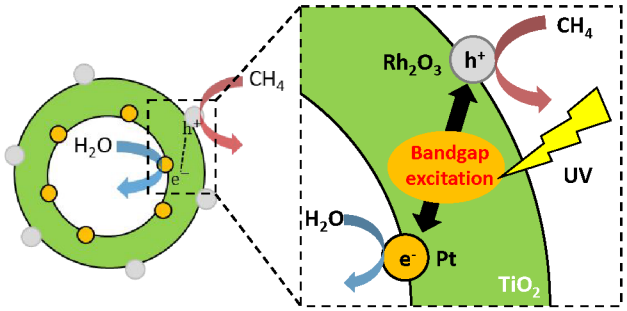

Scheme 2. Proposed reaction mechanism for photocatalytic SRM on Rh/hollow TiO_2/Pt. The UV irradiation triggers the bandgap excitation of TiO_2. The excited electrons are moved to Pt co-catalysts on the inner wall of hollow TiO_2, promoting H_2O reduction. In contrast, photo-excited holes are transferred to Rh_2O_3 on the outer surface to oxidize CH_4.

peak intensity and has the most efficient charge separation among the photocatalytic samples examined.

Based on the obtained action spectra and spectroscopic investigation results, a reaction mechanism was proposed for photocatalytic SRM on Rh/hollow TiO_2/Pt (**Scheme 2**). UV irradiation of Rh/hollow TiO_2/Pt results in bandgap excitation of hollow TiO_2 and the excited electrons and holes were moved to Pt sites on the inner surface and Rh_2O_3 sites on the outer surface, respectively, resulting in efficient charge separation. The photo-excited electrons on Pt sites were then consumed for H_2O reduction, whereas holes on Rh_2O_3 sites were used for CH_4 oxidation[37]. Although the possibility that CH_4 dissociation on Pt-TiO_2 cannot be ruled out, its contribution is limited judging from the fact that SRM activities on Pt/hollow TiO_2/Rh and Pt/hollow TiO_2/Pt are much smaller than those of Rh/hollow TiO_2/Pt and Rh/hollow TiO_2/Rh (Figure 3b), we concluded the contribution of methane dissociation on the Pt-TiO_2 is limited.

Conclusions

In the present work, hollow sphere-structured TiO_2 was fabricated to promote photocatalytic SRM. After loading with Pt and Rh as co-catalysts, the photocatalytic SRM activity of this material was largely enhanced. Notably, the highest H_2 production rate was achieved for the Rh/hollow TiO_2/Pt sample, in which Rh_2O_3 was loaded on the outer surfaces of hollow TiO_2 by a photodeposition method, whereas Pt was introduced on the inner TiO_2 surfaces using an impregnation method. In-situ ESR and PL measurements confirmed that photo-excited electrons were transferred to Pt sites, whereas holes were moved to Rh_2O_3 sites, thereby resulting in efficient charge separation. The present results are expected to aid in design strategies for more efficient photocatalytic methane conversion reactions.

Experimental Section

Characterization of TiO_2 samples

TiO_2 samples were characterized by X-ray diffraction (XRD) using a SmartLab X-ray diffractometer (Rigaku) with Cu Kα radiation (λ = 1.5418 Å). Sample morphology was observed by scanning electron microscopy (SEM, JCM-7000, JEOL) with an acceleration voltage of 15 kV. Characterization of the sample microstructures and elemental mapping of the Rh/hollow TiO_2/Pt samples were conducted by field emission transmission electron microscopy (FE-TEM, JEM-2010F, JEOL) with an acceleration voltage of 200 kV and also by transmission electron microscopy (TEM, JEM-ARM200F "NEO ARM", JEOL). Surface elemental analysis of Rh/Hollow TiO_2/Pt was conducted by field emission electron gun auger electron spectroscopy (AES, JAMP-9500F, JEOL). N_2 adsorption-desorption isotherms of hollow TiO_2 and Rh/hollow TiO_2/Pt were measured with a specific surface area/pore-distribution measurement instrument (Tristar II 3020, Shimadzu) at 77 K. To determine the pore size distribution and specific surface area of the samples, the Barrett-Joyner-Halenda (BJH) and Brunauer-Emmett-Teller (BET) methods, respectively, were used. The valence states of Rh, Pt, and Ti were examined with X-ray photoelectron spectroscopy (XPS, PHI-1600, ULVAC-PHI, Inc.) using Al Kα radiation as an X-ray source. For the analysis, samples were mounted on the holder with Cu tape, and binding energies were compensated with C 1s peak position (284.8 eV) and peaks were fitted with a Gaussian function. Ultraviolet-visible light (UV-Vis) absorption spectra were measured with a UV-Vis spectroscope (V-770, Jasco) using a diffuse reflectance method. Bandgap values were obtained using Tauc-plots, where $(F(R)h\nu)^{1/r}$ was plotted against photon energy ($h\nu$), where F(R), h, and ν represent Kubelka-Munk values obtained from the absorption spectra, Planck constant, and frequency of light, respectively. For the calculation, a value of r = 2 was applied because anatase TiO_2 causes indirect transition.

Photocatalytic SRM test

Photocatalytic SRM activities were examined under UV light irradiation with a 150 W Hg-Xe lamp (LA-410UV-5, Hayashi-Repic). The spectrum of the Hg-Xe lamp was obtained with a spectroradiometer (USR-45D, Ushio; Figure S9). For the SRM test, 15 mg powder samples were placed into a porous ceramic cup, which was then mounted in the flow-reactor equipped with a quartz window to allow light irradiation. A schematic image of the flow-reactor is shown in Figure S10. A gas mixture of Ar : CH_4 = 99 :1 vol.% was passed through precise humidity control equipment (me-39DPRT-MF-FH-SUS, Micro Equipment Inc.) to add 1.2 vol.% of water vapor into the gas mixture, which was then introduced into the flow-reactor at rate of 10 mL/min using a mass-flow controller. After purging the inside of the reactor with the reactant gas, the temperature was increased to 300 °C and UV irradiation was initiated. The produced gases (H_2, CO_2, and CO) were analyzed by micro-gas chromatography (MGC3000A, Inficon). The surface temperature of the powder sample was measured using a fiber-type radiation thermometer (TMHQ-CQE0500, Japan Sensor).

Action spectra for photocatalytic SRM were obtained using long-pass cutoff filters (300, 322, 385, 422, 450, and 470 nm; Hayashi-Repic) and the spectra of the Hg-Xe lamp using the filters are shown in Figure S11. PL spectra were obtained using a fluorescence

spectrophotometer (F-7000, HITACHI) with an excitation wavelength of 380 nm. In-situ ESR measurements were conducted using an operand electron spin resonance instrument (EMX nano, Bruker) under N_2 conditions at 100 K with UV light irradiation using an Hg-Xe lamp.

Author Contributions

A. Y.: Conceptualization, Supervision, Validation, Project administration, Writing-original draft. T. K.: Data curation, Formal Analysis, Investigation, Writing-review & editing. T. F.: Data curation, Formal analysis, Investigation, Writing-review & editing. H. A.: Formal analysis, Validation, Writing-review & editing. M. M.: Conceptualization, Supervision, Validation, Project administration, Writing-review & editing.

Conflicts of interest

There are no conflicts to declare.

Acknowledgements

This work was financially supported by JST CREST (Grant No. JPMJCR15P1). The XPS measurements were conducted with permission from the Equipment Sharing Management System of the Tokyo Institute of Technology. The authors also appreciate the Materials Analysis Division for assistance with the TEM observations and AES measurements. The authors thank Mr. Greg Newton for English language editing.

References

1 P. B. Euan G. Nisbet, Edward J. Dlugokencky, *Science (80-.).*, 2014, **343**, 493–495.
2 2013, 1, 1–244.
3 J. M. Lavoie, *Front. Chem.*, 2014, **2**, 1–17.
4 B. Cao, G. Li and H. Li, *Appl. Catal. B Environ.*, 2016, **194**, 42–49.
5 H. Arakawa, M. Aresta, J. N. Armor, M. A. Barteau, E. J. Beckman, A. T. Bell, J. E. Bercaw, C. Creutz, E. Dinjus, D. A. Dixon, K. Domen, D. L. DuBois, J. Eckert, E. Fujita, D. H. Gibson, W. A. Goddard, D. W. Goodman, J. Keller, G. J. Kubas, H. H. Kung, J. E. Lyons, L. E. Manzer, T. J. Marks, K. Morokuma, K. M. Nicholas, R. Periana, L. Que, J. Rostrup-Nielson, W. M. H. Sachtler, L. D. Schmidt, A. Sen, G. A. Somorjai, P. C. Stair, B. Ray Stults and W. Tumas, *Chem. Rev.*, 2001, **101**, 953–996.
6 S. B. Tang, F. L. Qiu and S. J. Lu, *Catal. Today*, 1995, **24**, 253–255.
7 C. J. Liu, J. Ye, J. Jiang and Y. Pan, *ChemCatChem*, 2011, **3**, 529–541.
8 T. da Silva Veras, T. S. Mozer, D. da Costa Rubim Messeder dos Santos and A. da Silva César, *Int. J. Hydrogen Energy*, 2017, **42**, 2018–2033.
9 J. Sehested, *Catal. Today*, 2006, **111**, 103–110.
10 J. R. Rostrup-Nielsen, *Catal. Today*, 1993, **18**, 305–324.
11 J. N. Armor, *Appl. Catal. A Gen.*, 1999, **176**, 159–176.
12 E. Huang, N. Rui, R. Rosales, P. Liu and J. A. Rodriguez, *J. Am. Chem. Soc.*, 2023, **145**, 8326–8331.
13 Y. Cho, A. Yamaguchi and M. Miyauchi, *Catalysts*, 2021, **11**, 1–41.
14 M. J. Fang, C. W. Tsao and Y. J. Hsu, *J. Phys. D. Appl. Phys.*, 2020, **53**, 143001.
15 C. W. Tsao, M. J. Fang and Y. J. Hsu, *Coord. Chem. Rev.*, 2021, **438**, 213876.
16 S. Wibowo, A. Yamaguchi, S. Shoji, T. Fujita, H. Abe and M. Miyauchi, *Chem. Lett.*, 2018, **47**, 935–937.
17 K. Takeda, A. Yamaguchi, Y. Cho, O. Anjaneyulu, T. Fujita, H. Abe and M. Miyauchi, *Glob. Challenges*, 2020, **4**, 1900067.
18 S. Shoji, X. Peng, A. Yamaguchi, R. Watanabe, C. Fukuhara, Y. Cho, T. Yamamoto, S. Matsumura, M. W. Yu, S. Ishii, T. Fujita, H. Abe and M. Miyauchi, *Nat. Catal.*, 2020, **3**, 148–153.
19 Y. Cho, S. Shoji, A. Yamaguchi, T. Hoshina, T. Fujita, H. Abe and M. Miyauchi, *Chem. Commun.*, 2020, **56**, 4611–4614.
20 M. Kushida, A. Yamaguchi, Y. Cho, T. Fujita, H. Abe and M. Miyauchi, *ChemPhotoChem*, 2021, **5**, 275–281.
21 S. Shoji, A. S. Bin Mohd Najib, M. W. Yu, T. Yamamoto, S. Yasuhara, A. Yamaguchi, X. Peng, S. Matsumura, S. Ishii, Y. Cho, T. Fujita, S. Ueda, K. P. Chen, H. Abe and M. Miyauchi, *Chem Catal.*, 2022, 2, 321–329.
22 M. Kushida, A. Yamaguchi and M. Miyauchi, *J. Energy Chem.*, 2022, **71**, 562–571.
23 H. Yoshida, S. Kato, K. Hirao, J. I. Nishimoto and T. Hattori, *Chem. Lett.*, 2007, **36**, 430–431.
24 H. Yoshida, K. Hirao, J. I. Nishimoto, K. Shimura, S. Kato, H. Itoh and T. Hattori, *J. Phys. Chem. C*, 2008, **112**, 5542–5551.
25 A. Yamamoto, S. Mizuba, Y. Saeki and H. Yoshida, *Appl. Catal. A Gen.*, 2016, **521**, 125–132.
26 H. Yoshida, S. Mizuba and A. Yamamoto, *Catal. Today*, 2019, **334**, 30–36.
27 B. V. Ayodele, A. A. Ghazali, M. Y. Mohd Yassin and S. Abdullah, *Int. J. Hydrogen Energy*, 2019, **44**, 20700–20710.
28 B. Han, W. Wei, M. Li, K. Sun and Y. H. Hu, *Chem. Commun.*, 2019, **55**, 7816–7819.
29 B. Tan, Y. Ye, Z. Huang, L. Ye, M. Ma and Y. Zhou, *Chinese Chem. Lett.*, 2020, **31**, 1530–1534.
30 A. Anzai, K. Fujiwara, A. Yamamoto and H. Yoshida, *Catal. Today*, 2020, **352**, 1–9.
31 W. Sarwana, A. Anzai, D. Takami, A. Yamamoto and H. Yoshida, *Catal. Sci. Technol.*, 2021, **11**, 5534–5542.
32 W. Sarwana, A. Yamamoto and H. Yoshida, *Catal. Today*, , DOI:10.1016/j.cattod.2022.07.026.
33 K. Shimura and H. Yoshida, *Energy Environ. Sci.*, 2010, **3**, 615–617.
34 K. Shimura, T. Yoshida and H. Yoshida, *J. Phys. Chem. C*, 2010, **114**, 11466–11474.
35 K. Shimura, S. Kato, T. Yoshida, H. Itoh, T. Hattori and H. Yoshida, *J. Phys. Chem. C*, 2010, **114**, 3493–3503.
36 H. Song, X. Meng, Z. J. Wang, Z. Wang, H. Chen, Y. Weng, F. Ichihara, M. Oshikiri, T. Kako and J. Ye, *ACS Catal.*, 2018, **8**, 7556–7565.

37 T. Kujirai, A. Yamaguchi, T. Fujita, H. Abe and M. Miyauchi, *Chem. Commun.*, 2021, **57**, 8007–8010.
38 M. Xiao, Z. Wang, M. Lyu, B. Luo, S. Wang, G. Liu, H. M. Cheng and L. Wang, *Adv. Mater.*, 2019, **31**, 1–23.
39 A. Meng, L. Zhang, B. Cheng and J. Yu, *Adv. Mater.*, , DOI:10.1002/adma.201807660.
40 D. Wang, T. Hisatomi, T. Takata, C. Pan, M. Katayama, J. Kubota and K. Domen, *Angew. Chemie - Int. Ed.*, 2013, **52**, 11252–11256.
41 D. Zheng, X. N. Cao and X. Wang, *Angew. Chemie - Int. Ed.*, 2016, **55**, 11512–11516.
42 A. Li, T. Wang, X. Chang, W. Cai, P. Zhang, J. Zhang and J. Gong, *Chem. Sci.*, 2016, **7**, 890–895.
43 Z. U. Rahman, N. Wei, M. Feng and D. Wang, *Int. J. Hydrogen Energy*, 2019, **44**, 13221–13231.
44 P. Zhang and X. W. (David) Lou, *Adv. Mater.*, 2019, **31**, 1–18.
45 X. Li, N. Li, Y. Gao and L. Ge, *Chinese J. Catal.*, 2022, **43**, 679–707.
46 S. Zhu, W. Liao, M. Zhang and S. Liang, *Chem. Eng. J.*, 2019, **361**, 461–469.
47 P. Luches, G. Gasperi, M. Sauerbrey, S. Valeri, J. Falta and J. I. Flege, *Front. Chem.*, 2019, **7**, 1–11.
48 P. Castro-Latorre, K. M. Neyman and A. Bruix, *J. Phys. Chem. C*, 2023, **127**, 17700–17710.
49 F. Zhang, R. A. Gutiérrez, P. G. Lustemberg, Z. Liu, N. Rui, T. Wu, P. J. Ramírez, W. Xu, H. Idriss, M. V. Ganduglia-Pirovano, S. D. Senanayake and J. A. Rodriguez, *ACS Catal.*, 2021, **11**, 1613–1623.
50 Y. Ao, J. Xu, D. Fu and C. Yuan, *Catal. Commun.*, 2008, **9**, 2574–2577.
51 K. S. W. Sing, D. H. Everett, R. A. W. Haul, L. Moscou, R. A. Pierotti, J. Rouquerol and T. Siemieniewska, *Int. UNION PURE Appl. Chem.*, 1985, **57**, 603–619.
52 M. Ojeda, M. L. Granados, S. Rojas, P. Terreros, F. J. García-García and J. L. G. Fierro, *Appl. Catal. A Gen.*, 2004, **261**, 47–55.
53 S. Suárez, M. Yates, A. L. Petre, J. A. Martín, P. Avila and J. Blanco, *Appl. Catal. B Environ.*, 2006, **64**, 302–311.
54 Y. V. Larichev, O. V. Netskina, O. V. Komova and V. I. Simagina, *Int. J. Hydrogen Energy*, 2010, **35**, 6501–6507.
55 K. Shimura, H. Kawai, T. Yoshida and H. Yoshida, *ACS Catal.*, 2012, **2**, 2126–2134.
56 F. Wang, R. J. Wong, J. H. Ho, Y. Jiang and R. Amal, *ACS Appl. Mater. Interfaces*, 2017, **9**, 30575–30582.
57 H. Choi, M. Carboni, Y. K. Kim, C. H. Jung, S. Y. Moon, M. M. Koebel and J. Y. Park, *Catal. Letters*, 2018, **148**, 1504–1513.
58 D. Kuscer, J. Kovač, M. Kosec and R. Andriesen, *J. Eur. Ceram. Soc.*, 2008, **28**, 577–584.
59 D. Reyes-Coronado, G. Rodríguez-Gattorno, M. E. Espinosa-Pesqueira, C. Cab, R. De Coss and G. Oskam, *Nanotechnology*, , DOI:10.1088/0957-4484/19/14/145605.
60 M. A. Henderson, *Surf. Sci. Rep.*, 2011, **66**, 185–297.
61 D. O. Scanlon, C. W. Dunnill, J. Buckeridge, S. A. Shevlin, A. J. Logsdail, S. M. Woodley, C. R. A. Catlow, M. J. Powell, R. G. Palgrave, I. P. Parkin, G. W. Watson, T. W. Keal, P. Sherwood, A. Walsh and A. A. Sokol, *Nat. Mater.*, 2013, **12**, 798–801.
62 N. Xiao, S. Li, X. Li, L. Ge, Y. Gao and N. Li, *Chinese J. Catal.*, 2020, **41**, 642–671.
63 J. Yang, D. Wang, H. Han and C. Li, *Acc. Chem. Res.*, 2013, **46**, 1900–1909.
64 T. Berger, M. Sterrer, O. Diwald, E. Knözinger, D. Panayotov, T. L. Thompson and J. T. Yates, *J. Phys. Chem. B*, 2005, **109**, 6061–6068.
65 R. Li, Y. Weng, X. Zhou, X. Wang, Y. Mi, R. Chong, H. Han and C. Li, *Energy Environ. Sci.*, 2015, **8**, 2377–2382.
66 Y. Alsalka, O. Al-Madanat, M. Curti, A. Hakki and D. W. Bahnemann, *ACS Appl. Energy Mater.*, 2020, **3**, 6678–6691.